Revised Version

EPJ manuscript No.
(will be inserted by the editor)

Measurement of the Electric Form Factor of the Neutron at $Q^2 = 0.3-0.8\ (\mathrm{GeV}/c)^2$

The A1 Collaboration

D.I. Glazier[2ab], M. Seimetz[1cd], J.R.M. Annand[2], H. Arenhövel[1], M. Ases Antelo[1], C. Ayerbe[1], P. Bartsch[1], D. Baumann[1], J. Bermuth[1], R. Böhm[1], D. Bosnar[6], M. Ding[1], M.O. Distler[1], D. Elsner[1e], J. Friedrich[1], S. Hedicke[1], P. Jennewein[1], G. Jover Mañas[1], F.H. Klein[1e], F. Klein[3], M. Kohl[4f], K.W. Krygier[1], K. Livingston[2], I.J.D. MacGregor[2], M. Makek[6], H. Merkel[1], P. Merle[1], D. Middleton[2], U. Müller[1g], R. Neuhausen[1], L. Nungesser[1], M. Ostrick[3], R. Pérez Benito[1], J. Pochodzalla[1], Th. Pospischil[1], M. Potokar[5], A. Reiter[2], G. Rosner[2], J. Sanner[1], H. Schmieden[1e], A. Süle[1e], Th. Walcher[1], D. Watts[2], M. Weis[1]

[1] Institut für Kernphysik, Johannes Gutenberg-Universität Mainz, Becherweg 45, 55099 Mainz, Germany
[2] Dept. of Physics and Astronomy, University of Glasgow, Glasgow G12 8QQ, UK
[3] Physikalisches Institut, Rheinische Friedrich-Wilhelms-Universität Bonn, Nussallee 12, 53115 Bonn, Germany
[4] Institut für Kernphysik, Technische Universität Darmstadt, Schlossgartenstraße 9, 64289 Darmstadt, Germany
[5] Institute "Jožef Stefan", University of Ljubljana, Jamova 39, 1000 Ljubljana, Slovenia
[6] Department of Physics, University of Zagreb, Bijenička c. 32, P.P. 331, 10002 Zagreb, Croatia

Received: date / Revised version: date

Abstract. The electric form factor of the neutron, $G_{E,n}$, has been measured at the Mainz Microtron by recoil polarimetry in the quasielastic $\mathrm{D}(\vec{e},e'\vec{n})p$ reaction. Three data points have been extracted at squared four-momentum transfers $Q^2 = 0.3,\ 0.6$ and $0.8\ (\mathrm{GeV}/c)^2$. Corrections for nuclear binding effects have been applied.

PACS. 13.40.Gp Electromagnetic form factors – 14.20.Dh Protons and neutrons – 13.88.+e Polarisation in interactions and scattering

arXiv:nucl-ex/0410026 v2 6 Dec 2004

1 Introduction

The Sachs elastic electromagnetic form factors parametrise the nucleon's ability to absorb transferred four-momentum, Q^2, without excitation or particle emission. They are interpreted as the Fourier transforms of the distributions of charge and magnetisation inside the nucleon [1,2] and may be linked to other observables, such as polarisabilities or DIS structure functions, through the framework of Generalised Parton Distributions (GPD) [3]. The elastic form factors offer a stringent test of any nucleon structure model. Furthermore a precise knowledge of the Q^2 dependence of the form factors is a prerequisite for the interpretation of other electromagnetic reactions such as parity-violating $\vec{e}$-p scattering and electron-nucleus scattering.

Thus high precision nucleon form factor measurements are necessary, but the electric form factor of the neutron, $G_{E,n}$, is particularly difficult to access, due to its small magnitude and the lack of free neutron targets. Using light nuclear targets, D and ^{3}He, it can be obtained via interference terms where the small $G_{E,n}$ is multiplied by the much larger $G_{E,p}$ or $G_{M,n}$ form factors. The product $G_{E,n}G_{E,p}$ may be accessed in *elastic* $\mathrm{D}(e,e')$ scattering. Precision measurements [4] provided $G_{E,n}$ data showing a Q^2 dependence that can be parametrized by the Galster form [5]. However these data have large systematic errors, mainly due to the model dependent uncertainties in unfolding the deuteron wavefunction contribution to the cross section. Subsequently, reduced model dependence has been achieved from the analysis of measurements of the quadrupole form factor, extracted using polarisation data [6]. Alternatively, uncertainty in model dependent corrections can be reduced, and in some cases almost eliminated, by measuring asymmetries in double-polarised, quasi-free $(e,e'n)$ reactions which yield terms proportional

[a] Comprises part of Ph.D. thesis
[b] e-mail: d.glazier@physics.gla.ac.uk
[c] Comprises part of doctorate thesis
[d] Now at: DAPNIA/SPhN, CEA Saclay, 91191 Gif sur Yvette Cedex, France, e-mail: mseimetz@cea.fr
[e] Now at: Physikalisches Institut, Rheinische Friedrich-Wilhelms-Universität Bonn, Germany
[f] Now at: MIT-Bates Linear Accelerator Center, Middleton, USA
[g] e-mail: ulm@kph.uni-mainz.de

to the product $G_{E,n}\,G_{M,n}$. Three methods have been used to obtain $G_{E,n}$: $\mathrm{D}(\vec{e},e'\vec{n})p$ [7,8,9,10], $\vec{\mathrm{D}}(\vec{e},e'n)p$, [11,12, 13], and $^3\vec{\mathrm{He}}(\vec{e},e')$ [14,15]. Bound nucleon corrections, particularly at small Q^2, are larger and inherently more difficult to calculate for ^{3}He.

The $G_{E,n}$ experiment described here measured the polarisation transfer to the neutron in the $\mathrm{D}(\vec{e},e'\vec{n})p$ reaction. The feasibility of the technique was already demonstrated at MIT-Bates [7,16]. Using the high current, high polarisation, 100% duty factor electron beam of the Mainz Microtron (MAMI), the statistical precision could be improved by an order of magnitude. Moreover, the absolute calibrations of electron beam polarisation and analysing power of the neutron polarimeter were avoided by implementing neutron spin precession in an appropriate magnetic field [8]. Thus this technique, which is explained in sect. 2, eliminated two major sources of systematic uncertainty.

Effects of the nuclear binding of the neutron in the deuteron were corrected for using the model of Arenhövel *et al.* [17]. This model has proven highly successful in describing electron scattering on the deuteron, so that a small relative error in the correction could be assumed. In spite of the corrections' sizeable contribution to the final $G_{E,n}$ values, their contribution to the systematic uncertainty in $G_{E,n}$ is small.

The following sections provide a description of the experimental technique and data analysis, a presentation of the present results along with a comparison with previous double-polarisation data, and a brief comparison with recent nucleon model calculations.

2 Experimental method

2.1 Principle of measurement

In polarised electron-nucleon scattering, $N(\vec{e},e'\vec{N})$, the polarisation transfer is favourably expressed in the electron scattering plane, which is spanned by the unit vectors

$$\widehat{\boldsymbol{z}}=\widehat{\boldsymbol{q}},\;\; \widehat{\boldsymbol{y}}=\frac{\boldsymbol{p_e}\times\boldsymbol{p_e'}}{\left|\boldsymbol{p_e}\times\boldsymbol{p_e'}\right|},\;\; \widehat{\boldsymbol{x}}=\widehat{\boldsymbol{y}}\times\widehat{\boldsymbol{z}}\;, \tag{1}$$

as depicted in fig. 1. The ratio of the non-vanishing nucleon polarisation components is given by [18,19]

$$R_{\mathcal{P}}=\frac{\mathcal{P}_x}{\mathcal{P}_z}=-\frac{1}{\sqrt{\tau+\tau(1+\tau)\tan^2\vartheta_e/2}}\cdot\frac{G_{E,N}}{G_{M,N}}\;, \tag{2}$$

where $\tau=Q^2/4M_N^2c^2$ denotes the dimensionless four momentum transfer from the electron to the target nucleon, M_N is the nucleon mass, and ϑ_e is the electron scattering angle in the laboratory frame. This formula describes the case of a nucleon initially free and at rest. The best approximation to this situation is offered by the quasi-free $\mathrm{D}(\vec{e},e'\vec{n})p$ reaction. Nuclear binding effects are small, provided that the momentum transfer is large compared to the nucleons' Fermi-momenta. Corrections for these effects are detailed in sect. 3.3.

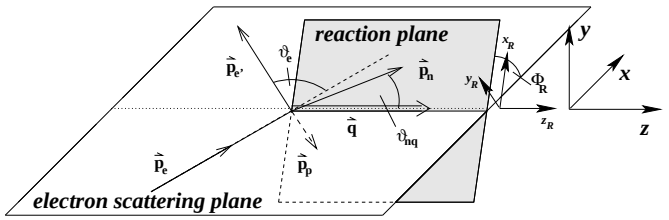

Fig. 1. Definition of the reaction plane, which is spanned by the momenta of the outgoing nucleons. The final state neutron is described in the coordinate system (x_R, y_R, z_R).

Neutron polarimetry exploits the spin-orbit dependence of the strong interaction in scattering reactions of polarised neutrons on target nuclei. The cross section dependence on the azimuthal scattering angle Φ_n is related to the polarisation component transverse to the neutron momentum, $\mathcal{P}_t$. It is possible to use plastic scintillator material, commonly used in neutron detectors, as active neutron scatterer, what allows the reconstruction of the interaction vertex [20]. If $\mathcal{P}_t\equiv\mathcal{P}_x$ (as for an initially free nucleon at rest) the polarised neutron scattering exhibits an 'up-down' asymmetry, A, in the Φ_n distribution, which may be measured with a second scintillator wall. It shows a sinusoidal dependence on Φ_n, with an amplitude dependent on the analysing power of the first interaction, averaged over the detector acceptancies, $\mathcal{A}_{\mathrm{eff}}$:

$$\begin{aligned}A&=\frac{\sqrt{N^+(\Phi_n)N^-(\Phi_n+\pi)}-\sqrt{N^+(\Phi_n+\pi)N^-(\Phi_n)}}{\sqrt{N^+(\Phi_n)N^-(\Phi_n+\pi)}+\sqrt{N^+(\Phi_n+\pi)N^-(\Phi_n)}}\\&=\mathcal{A}_{\mathrm{eff}}\mathcal{P}_t\sin\Phi_n\;.\end{aligned} \tag{3}$$

$N^h(\Phi_n)$ and $N^h(\Phi_n+\pi)$ indicate the number of neutrons detected in a bin around Φ_n $(0<\Phi_n<\pi)$ and $\Phi_n+\pi$, respectively, and with a beam helicity $h=\pm1$. This expression exploits the spin flip of the ejected nucleon in free $(\vec{e},e'\vec{n})$ scattering under helicity reversal of the electron beam and gives a measurement independent of the neutron detection efficiency and of the luminosity.

The need for absolute calibrations of the electron beam polarisation, P_e, and the effective analysing power, $\mathcal{A}_{\mathrm{eff}}$, can be circumvented by measuring the polarisation ratio $\mathcal{P}_x/\mathcal{P}_z$ directly. This method was first utilised by the A3 collaboration at MAMI [8]. In order to become sensitive to both the transverse and longitudinal polarisation components, the neutron spin is precessed in a magnetic field perpendicular to the electron scattering plane. The transverse polarisation of the neutron after a precession through angle χ is given in terms of the initial polarisation components (with $\mathcal{P}_y=0$) by

$$\mathcal{P}_t=\mathcal{P}_x\cos\chi-\mathcal{P}_z\sin\chi=\mathcal{P}_0\sin(\chi-\chi_0)\,, \tag{4}$$

where $\mathcal{P}_0=\sqrt{\mathcal{P}_x^2+\mathcal{P}_z^2}$. The precession by an angle χ_0 which yields a vanishing $\mathcal{P}_t$ and hence zero asymmetry is directly related to the form factor ratio through

$$\tan\chi_0=R_{\mathcal{P}}\;. \tag{5}$$

As the angle χ_0 is independent of the analysing power and the absolute value of the electron beam polarisation, only relative fluctuations of P_e have to be monitored when measuring asymmetries for a number of different precession angles.

2.2 Experimental Setup

The $\mathrm{D}(\vec{e},e'\vec{n})p$ experiment was carried out at the Three Spectrometer Facility of the A1 collaboration at the Mainz Microtron, MAMI [21]. The polarisation of the incoming electron beam was measured regularly with a Møller polarimeter, and was found to be close to 80%. The polarised beam, with currents of 10–15 μA, was scattered from a liquid deuterium target of 5 cm length. Spectrometer A was used to detect the scattered electrons. Its momentum resolution $\Delta p/p \leq 10^{-4}$ and angular resolution $\Delta\varphi, \Delta\vartheta \leq 3$ mrad allowed for a precise reconstruction of the virtual photon four-momentum, q. Data were taken at three central momentum transfers, $Q^2 = 0.3$, 0.6 and 0.8 $(\mathrm{GeV}/c)^2$. The electron beam energy, as well as the central angles of spectrometer A and of the neutron polarimeter, were different in each case. Table 1 summarises the kinematics. The pure data taking time amounted to 55 days in 2001, and 52 days in 2002.

Table 1. Kinematics of the A1 $G_{E,n}$ experiment. E'_e and T_n are the central energies of the outgoing electron and neutron, respectively. The angles ϑ_e^c and ϑ_n^c are the central angles of the detectors.

$Q^2/(\mathrm{GeV}/c)^2$	0.3	0.6	0.8	
E_e/MeV	660	855	883	
E'_e/MeV	498	536	454	Spectrometer A
ϑ_e^c	57°	70°	90°	
T_n/MeV	160	320	427	Neutron
ϑ_n^c	47°	37°	27°	polarimeter

The neutrons were detected in coincidence with the scattered electrons. They passed through a dipole magnet, positioned 3 m from the target, the vertical field of which precessed the neutron spin about a vertical axis. Analysis scattering of the neutrons took place in a two-layer array of plastic scintillators (fig. 3), each containing 15 vertically aligned bars ($5 \times 80 \times 7.5$ cm^3). This first wall was positioned 6 m from the target and covered a solid angle of ~ 17 msr. The light signals from both ends of the scintillator bars were recorded, allowing reconstruction (by time difference) of the hit position along the length of each bar. Combined with the 5 cm width of the bars this resulted in an angular resolution of 0.5° FWHM. The scintillators of the second wall ($180 \times 20 \times 10$ cm^3) were arranged horizontally in two blocks above and below the electron scattering plane at a distance 3 m from the first wall. Charged particles were identified by a layer of thin plastic scintillators in front of each wall of the polarimeter. The first particle-identification (veto) layer consisted of 15 elements of size $7.5 \times 81 \times 1$ cm^3, while the rear was constructed from 4 elements per block, of size $180 \times 20 \times 1$ cm^3.

The rear wall detectors were shielded from direct target view by the massive iron yoke of the spin precession magnet. In addition a 5 cm thick lead wall, located in the gap of the spin precession magnet, attenuated mainly low energy electromagnetic background from the target region, which was necessary to maintain the front-wall single rates at manageable levels (< 1 MHz). In order to investigate the effect of the lead shielding on the polarisation of traversing nucleons, $p(\vec{e},e'\vec{p})$ measurements using the focal plane proton polarimeter [22] of spectrometer A have been performed. No indication for any degradation of the polarisation has been obtained for protons with kinetic energies $T_p \simeq 200$–350 MeV and shielding lengths up to 6 cm [23]. A 1 m thick concrete wall, stacked to a height of 5.5 m, shielded the entire polarimeter from the exit beam line and beam dump.

Full details of the neutron polarimeter will be given in a future publication [24].

3 Data analysis

3.1 Selection of quasielastic $\mathrm{D}(\vec{\mathrm{e}},\mathrm{e}'\vec{\mathrm{n}})\mathrm{p}$ events

The following observables, measured in the neutron polarimeter and spectrometer A, were relevant for the reconstruction of the deuteron breakup reaction: The neutrons' angles, (ϑ_n, φ_n), and time-of-flight, T_1, to the first wall and the scattering angles, (ϑ_e, φ_e), and energy, E'_e, of the electrons. By detecting both particles in coincidence the kinematics of the $\mathrm{D}(\vec{e},e'\vec{n})p$ event was reconstructed. Since deuteron electrodisintegration can be fully described with five variables we made use of the sixth for the definition of kinematic constraints. For each event the expected neutron time-of-flight, denoted by T_A, as calculated from the set of observables (E'_e, ϑ_e, φ_e, ϑ_n, φ_n), was compared to the measured time, T_1. While the distribution of neutron flight times is broad due to Fermi motion and the finite acceptances of the spectrometer and of the polarimeter, the variable $\Delta T_{1,A} := T_1 - T_A$ has a much narrower distribution which identifies quasielastic events with good signal-to-noise ratio (fig. 2).

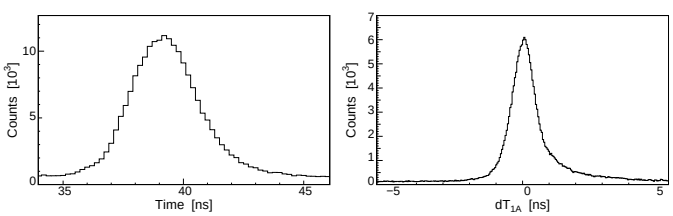

Fig. 2. Left: Measured flight time T_1 to the first scintillator wall, relative to the electron arrival time in spectrometer A, for $Q^2 = 0.3$ $(\mathrm{GeV}/c)^2$. Right: The difference $\Delta T_{1,A}$ between T_1 and the calculated neutron time-of-flight T_A.

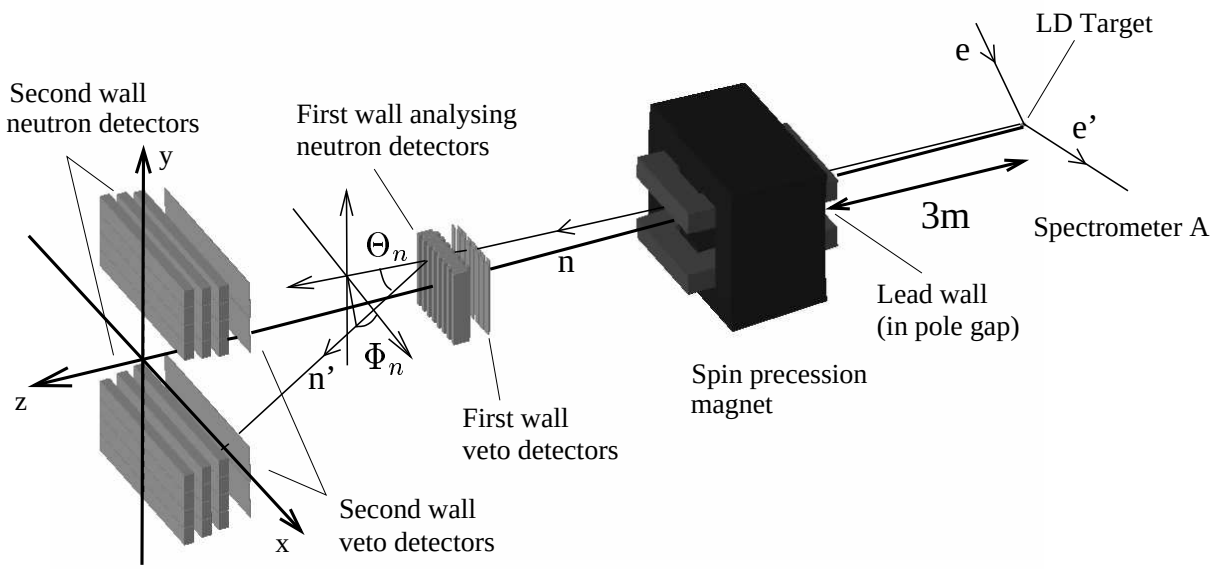

Fig. 3. Three dimensional view of the A1 neutron polarimeter.

D$(e,e'n)p$ events were identified as follows: π^- were rejected using threshold Čerenkov information of spectrometer A; the $(e,e'n)$ interaction vertex was constrained to be inside the target cell; an e'-n coincidence was required. On the first wall of the polarimeter times-of-flight were constrained to be consistent with D$(e,e'n)p$ kinematics.

3.2 Neutron scattering in the polarimeter

In addition to the observables listed in sec. 3.1 the scattering angles, (Θ_n, Φ_n), of particles scattered in the first scintillator wall and their time-of-flight, T_{12}, to the second wall have been measured. The analysing power, $\mathcal{A}$, of elastic n-p scattering is a function of the neutron scattering angle and kinetic energy. In fig. 4, $\mathcal{A}$ is shown for the three central energies associated with our measured Q^2 values (table 1). In addition to elastic n-p scattering, various inelastic n-C reactions in the mainly CH_2 scintillator material have an important contribution to the observed $(\vec{n},n')$ yield. At neutron kinetic energies of a few hundred MeV the quasielastic C(n,nN) channels dominate the cross section and have a Θ_n dependence in analysing power similar to the free n-p scattering case and therefore contribute positively to the overall effective analysing power of the polarimeter. The cross sections and analysing powers of these channels are not precisely known, and as a result $\mathcal{A}_{\rm eff}$ cannot be calculated accurately. Although the spin precession technique removes the need for an accurate value of $\mathcal{A}_{\rm eff}$, the attainable statistical precision in asymmetry measurements depends strongly on this quantity.

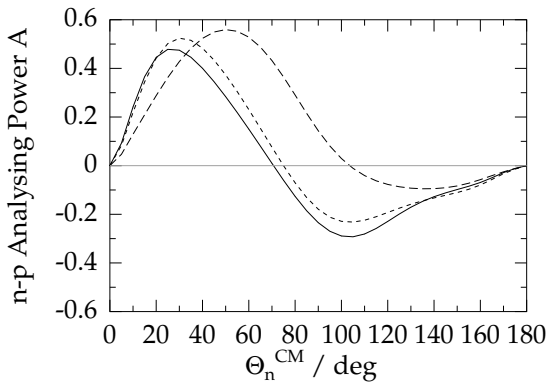

Fig. 4. Analysing power of elastic n-p scattering, plotted against the neutron scattering angle $\Theta_n^{\rm CM}$ in the center-of-mass system for three different neutron energies, T_n = 160 (long dashed), 319 (short dashed), and 425 MeV (full curve). Data are taken from SAID [25].

Two kinematically distinct regions, corresponding to forward and backward n-p scattering, are accessible in our polarimeter.

1. Neutrons scattered at forward angles transfer only a minor part of their kinetic energy to the recoiling protons. The scattered neutrons are detected in the rear scintillator wall, while the 10–60 MeV recoil protons are mostly stopped in the front wall. In this case the proton energy deposition in the front scintillators is correlated with the measured time-of-flight of the neutrons between the first and second walls. Since the neutrons are detected twice these hits will be noted nn events in the following.

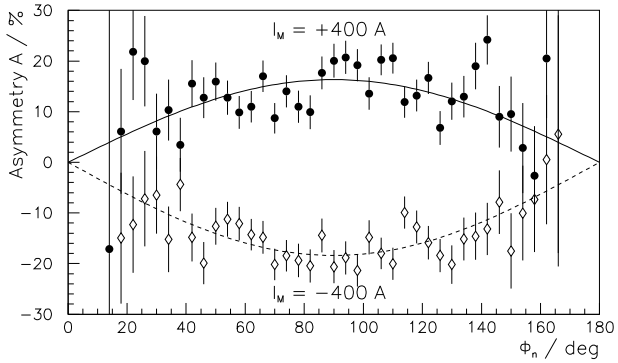

Fig. 5. The asymmetry A for nn events, plotted against the azimuthal scattering angle Φ_n, for two opposite orientations of the spin precessing field at magnet currents of $I_M = \pm 400$ A (field integral 1.1 Tm, $Q^2 = 0.3$ (GeV/c)^2). The curves are one-parameter sine fits: $A = A_0 \sin \Phi_n$.

2. The neutron scatters at backward angles and the energetic forward going recoil proton is detected in the rear scintillator wall. These np events have a negative analysing power (fig. 4) with respect to nn events, but since the azimuthal angle of detected protons differs from that of the neutrons by 180° the measured up-down asymmetries have the same sign as for the nn case.

Thus we have two statistically independent and, through the charged-particle identification in the rear wall, clearly distinct data sets in our analysis. Both sets have comparable statistical errors despite a smaller $\mathcal{A}_{\rm eff}$ in the np sample due to the 100% detection efficiency for the protons (see sect. 4.1). The thin scintillator layers were used to determine charged or uncharged hits in the front and rear walls. Charged hits in the front wall were rejected while the charged-uncharged decision at the rear wall gated the filling of the np or nn samples. The effect of proton or neutron misidentification was carefully studied (sec. 4.1).

Polarimeter analysis was complicated by the large number of events containing multiple hits. Where these occured in adjacent scintillator bars we assumed they resulted from a single particle and averaged the spatial information to reconstruct the interaction vertex. In the case of hits in separated detector elements (*e.g.* in the top and bottom parts of the second wall) separate particles were assumed. In such cases all possible combinations of hits in the two scintillator walls were analysed as different events and double-counting was then corrected for in the background subtraction procedure. The neutron time-of-flight spectra showed prominent signals on top of a random background and random events were selected from unphysical time-of-flight regions, well separated from the signal region.

Asymmetries A, eq. (3), were generated using the $N^h(\Phi_n)$ distributions and are shown in fig. 5 for the biggest spin precession angles.

The zero crossing angle, χ_0, obtained from the χ dependence of the asymmetry (eq.s (3) and (4)), is independent of the absolute value of the electron beam polarisation, P_e, provided this remains constant. The asymmetries at single χ values depend on P_e at the time of measurement. Systematic drifts of the beam polarisation were observed only over time scales of several days. Since we changed the magnetic field setting every four hours the average polarisations of all seven settings are nearly equal. The small observed fluctuations in the mean P_e at the 0.2% level, *i.e.* within the systematic uncertainty of the Møller polarimeter [26], were factored into $A(\chi_i)$ before χ_0 was determined.

3.3 Correction of nuclear binding effects

The relation (2) between the polarisation components of the recoil neutron and the Sachs form factors holds exactly for elastic scattering of polarised electrons from free nucleons. However in the case of quasielastic scattering, the binding and Fermi motion of the neutron in the deuteron lead to deviations from the free case. The number of independent kinematic variables increases from two to five as already mentioned in sect. 3.1. Due to Fermi motion, the recoil neutron is not necessarily ejected in the electron scattering plane, but rather in a reaction plane, which is rotated with respect to the electron scattering plane by an angle Φ_R about the direction of momentum transfer, $\hat{\mathbf{q}}$ (fig. 1). We measured the polarisation transverse to the outgoing neutron momentum, and the polarisation components in this frame, $\mathcal{P}_x^R$ and $\mathcal{P}_z^R$, are related to those in eq. (2) through a Wigner rotation. The Wigner angle, ϑ_W, is closely related to the angle ϑ_{nq} between the direction of $\hat{\mathbf{q}}$ and $\hat{\mathbf{p}}_\mathbf{n}$. This purely kinematical effect cancels in cases where the polarimeter acceptance is perfectly 180°-symmetric around $\hat{\mathbf{q}}$. However, as shown in [8], small deviations from this ideal situation can be corrected for by use of a single parameter, $f := \sin\vartheta_W \cos\Phi_R \ll 1$, which is calculated for each event. The polarisation ratios in the electron scattering and reaction planes are related via

$$\frac{\mathcal{P}_x}{\mathcal{P}_z} = \frac{\mathcal{P}_x^R}{\mathcal{P}_z^R} + \bar{f}\left(1 + \left(\frac{\mathcal{P}_x^R}{\mathcal{P}_z^R}\right)^2\right) + \mathcal{O}(\bar{f}^2)\,, \qquad (6)$$

using the mean value $\bar{f}$ of the f distribution.

Even in quasifree kinematics, nuclear binding effects and final state interactions (FSI) can lead to a reduction of the polarisation ratio compared to the free case. This is especially significant at $Q^2 < 0.3$ (GeV/c)^2. The effects of FSI, meson exchange currents (MEC), and isobar configuration currents (IC) on the polarisation components have been calculated in a model by Arenhövel *et al.* [17]. In order to incorporate these results into our analysis we applied a method similar to that developed by the A3 collaboration [9]. $R_\mathcal{P}$, eq. (2), was calculated for every accepted event for both the free ("Born" case) and the initially bound (labelled "FSI") neutrons. The measured zero crossing point of the neutron asymmetries was then shifted by

$$\Delta(\tan\chi_0) = \left(\frac{\mathcal{P}_x}{\mathcal{P}_z}\right)_{\rm Born} - \left(\frac{\mathcal{P}_x}{\mathcal{P}_z}\right)_{\rm FSI}\,. \qquad (7)$$

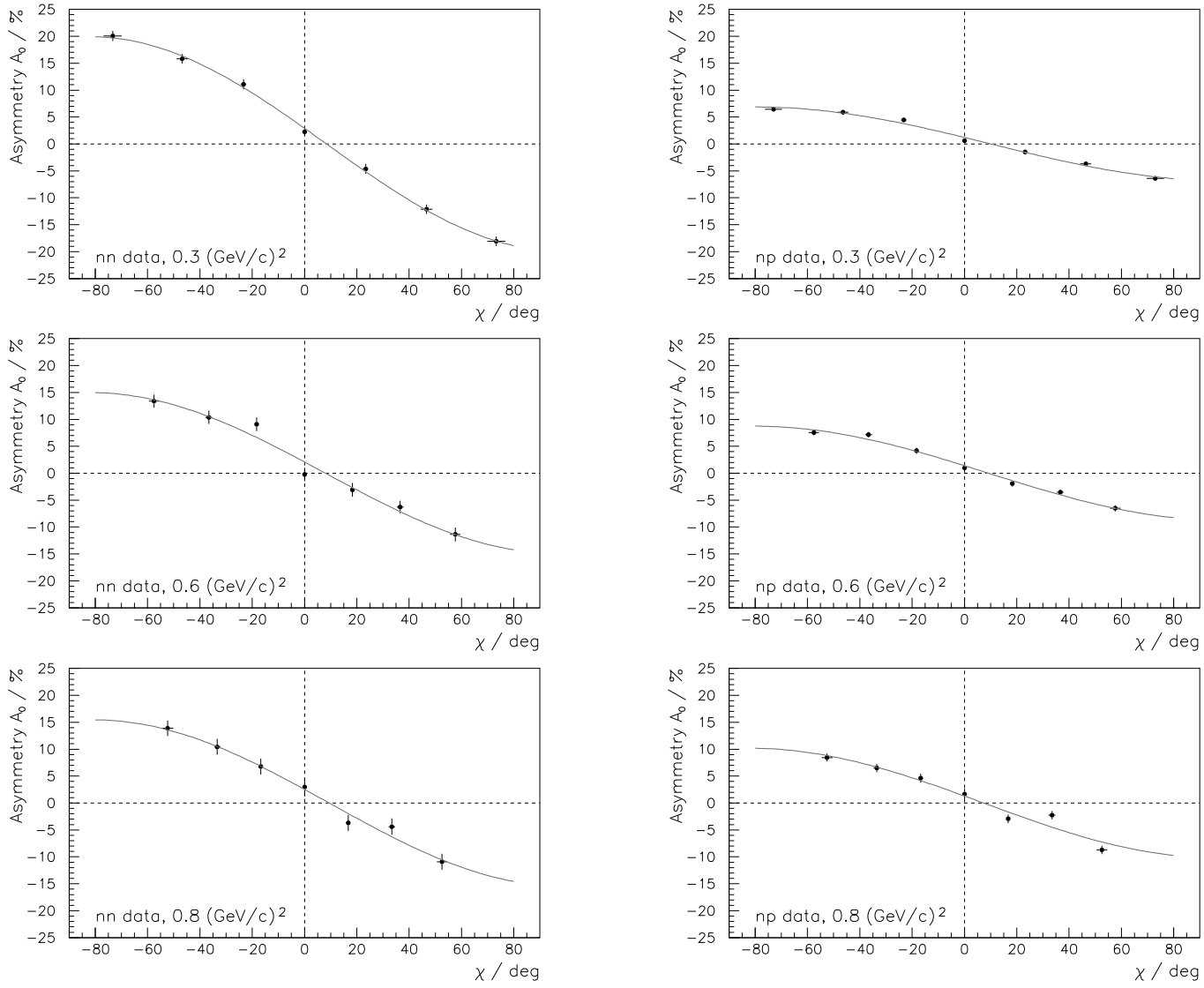

Fig. 6. Fit of the zero crossing point at (from top to bottom) $Q^2 = 0.3$, 0.6 and 0.8 $(\mathrm{GeV}/c)^2$. *nn* events are shown on the left, *np* events on the right hand side. Horizontal error bars represent the uncertainties in χ (see text).

The effect of the weak dependence of the corrections on the input value for $G_{E,n}$ was estimated by varying this value in the model over a reasonable range.

4 Results

4.1 Measured data points

In fig. 6 we show the measured χ dependence of the azimuthal asymmetries A_0 for the momentum transfers $Q^2 = 0.3$, 0.6 and 0.8 $(\mathrm{GeV}/c)^2$ and for the *nn* and *np* data samples. The zero crossing points χ_0 were obtained via two-parameter sine fits: $A_0 = A_0^0 \sin(\chi - \chi_0)$. The asymmetries were larger in the *nn* case due to the larger analysing power of this channel. However, the statistical errors on the extracted χ_0 values are of similar size for the *nn* and *np* samples due to the larger number of detected *np* events. The results of the fits as well as the acceptance and nuclear binding corrections are shown in table 2.

The extraction of $G_{E,n}$ through eq. (2) requires the knowledge of the magnetic form factor at the given Q^2 and of the kinematic factor

$$F := -[\tau + \tau(1+\tau)\tan^2\vartheta_e/2]^{-1/2} \ . \qquad (8)$$

The former was taken from a recent parametrisation [27] which gives a good representation of $G_{M,n}$ throughout our Q^2 range. It is based on data obtained from five experiments and quotes a relative error of $\Delta G_{M,n}/G_{M,n} \simeq 1.1\%$. The factor $G_{M,n} \cdot F$ was calculated for each event and then averaged over the acceptance.

Our final $G_{E,n}$ values were obtained from the mean values for the *nn* and *np* samples taken at the same Q^2. They are summarised in table 2.

Table 2. Results for the nn and np data samples at the three Q^2 values (the ranges in Q^2 represent the experimental acceptance): Numbers of accepted events, N_n, asymmetry amplitudes, A_0^0, and the results for $G_{E,n}$ extracted from this experiment. Values for $G_{E,n}$ are given for an evaluation of the uncorrected asymmetries, $G_{E,n}^{\text{uncorr.}}$, for an analysis accounting for the kinematic corrections of nuclear binding effects via eq. (6), $G_{E,n}^{\text{kin. corr.}}$, and for the final results, $G_{E,n}^{\text{full corr.}}$, where also the FSI corrections, eq. (7), have been taken into account. The last column contains the combined results of the nn and np samples.

$Q^2/(\text{GeV}/c)^2$	sample	N_n	$A_0^0 \cdot 100$	$G_{E,n}^{\text{uncorr.}}$	$G_{E,n}^{\text{kin. corr.}}$	$G_{E,n}^{\text{full corr.}} \pm \Delta G_{E,n}^{\text{stat}}$	$G_{E,n} \pm \Delta G_{E,n}^{\text{stat}} \pm \Delta G_{E,n}^{\text{syst}}$
0.30 ± 0.02	nn	114000	19.9 ± 0.5	0.0458	0.0447	0.0520 ± 0.0077	$0.0552 \pm 0.0061^{+0.0018}_{-0.0011}$
0.30 ± 0.02	np	570000	6.9 ± 0.5	0.0555	0.0524	0.0607 ± 0.0100	
0.59 ± 0.03	nn	55000	15.0 ± 0.8	0.0413	0.0408	0.0437 ± 0.0116	$0.0477 \pm 0.0070^{+0.0019}_{-0.0008}$
0.59 ± 0.03	np	316000	8.8 ± 0.4	0.0475	0.0469	0.0500 ± 0.0088	
0.79 ± 0.03	nn	86000	15.4 ± 1.0	0.0526	0.0519	0.0545 ± 0.0146	$0.0468 \pm 0.0090^{+0.0025}_{-0.0010}$
0.79 ± 0.03	np	204000	10.2 ± 0.5	0.0402	0.0396	0.0420 ± 0.0116	

The systematic errors are not symmetric since background events due to misidentified protons may cause asymmetries with signs opposite to the ones expected for neutrons. Protons may be misidentified in the first scintillator wall for two reasons. First of all, even though charged particles are eliminated with the use of veto detectors and additional offline hit pattern conditions this filtering may not be 100% efficient. Secondly, charge-exchange reactions in the lead shielding may result in p-n conversion. In order to estimate the magnitude of these effects data taken with an LH_2 target have been analysed applying the same event selection conditions as for the LD_2 data, and possible asymmetries caused by the false-identified neutron events have been estimated conservatively assuming that all misidentified protons were polarised according to eq. (2). Due to limited statistics a direct extraction of false asymmetries from the LH_2 data was not feasible. Therefore the "worst-case" estimate is considered as contribution to the error in the determination of $G_{E,n}$, rather than as a correction term. It is given in table 3 along with the other sources of systematic uncertainty.

As mentioned above, small fluctuations of the beam polarisation have been corrected for in the data analysis. Uncertainties in the neutron precession angles, resulting from field inhomogeneities, the absolute calibration of the field integrals, and the finite acceptance in neutron velocities have been included as ordinate errors in the fit procedure of the zero crossing points. The influence of radiative corrections on the extracted form factor ratio is estimated on basis of the calculation of Afanasev *et al.* [28] to be well below the one percent level.

Our results are shown as crosses in fig. 7 together with published $G_{E,n}$ values from other double-polarisation experiments. The new data points at $Q^2 = 0.3$, 0.6 and 0.8 $(\text{GeV}/c)^2$ agree well with those of the previous measurements. Some $G_{E,n}$ data points have been superseded and therefore are not shown here. This holds *e.g.* for the pilot experiment of the A3 collaboration [29], which was later repeated with much better statistics [14]. FSI corrections, which are sizeable for $^3\vec{\text{He}}$ at low Q^2, were applied to these results *a posteriori* in an independent publication [30], which, in turn, ignored the systematic experimental errors. The respective A3 data point included in fig. 7 is the FSI-corrected result from [30], but with the systematic errors from the original paper [14] added, which gives a fair representation of the results of that experiment.

Table 3. Systematic errors in the extraction of $G_{E,n}$. The quoted ranges cover the three Q^2 values.

Error source	$\Delta G_{E,n}/G_{E,n}$
$G_{M,n}$	1.1%
$F \cdot G_{M,n}$	0.9%
Remaining proton background	2.5–5.0%
FSI corrections	0.7–1.4%
total	3.0–5.2%

4.2 Phenomenological Fits

The thin full line in fig. 7 shows the simple $G_{E,n}$ parametrisation given by Galster *et al.* in 1971 [5],

$$G_{E,n}(Q^2) = -\frac{\mu_n \tau}{1 + p\tau} G_D(Q^2) \qquad (9)$$

with the usual dipole form factor G_D. It was purely phenomenological and contained only one free parameter, which was determined at that time from data up to 1 $(\text{GeV}/c)^2$ to be $p = 5.6$. This fit is still in reasonable agreement with the recent double-polarisation data, but considering the large uncertainties in the data available in 1971, this has to be regarded as coincidental.

Recently the low Q^2 dependence of the Sachs form factors has been interpreted [31] as direct evidence for a pion cloud surrounding the bare nucleon. The thick, full curve in fig. 7 represents the phenomenological parametrisation of ref. [31], showing a bump, characteristic of the pion cloud, at $Q^2 \simeq 0.25\ (\text{GeV}/c)^2$. It has the form

$$G_N(Q^2) = G_s(Q^2) + a_b \cdot Q^2 G_b(Q^2)\ , \qquad (10)$$

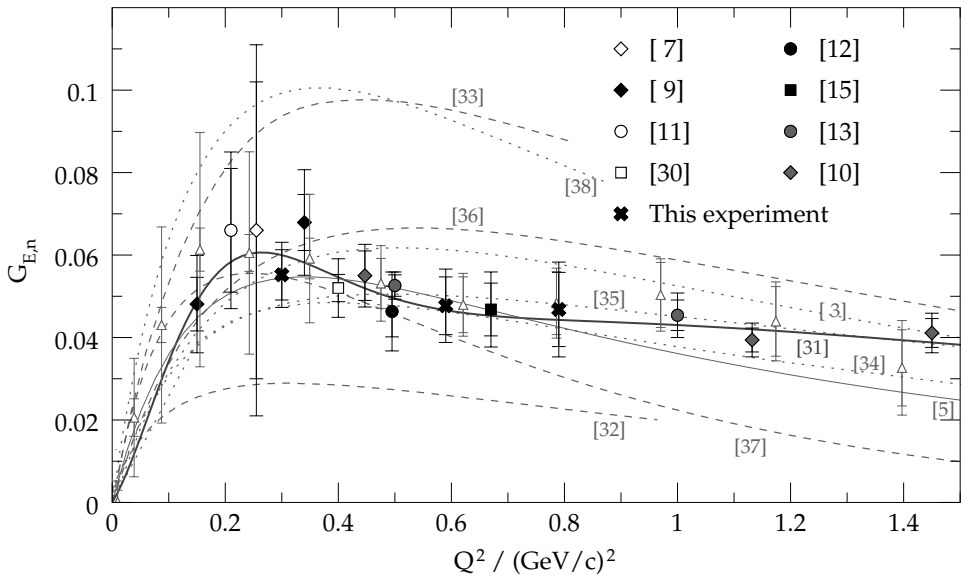

Fig. 7. $G_{E,n}$ from double-polarisation experiments. Polarisation-transfer measurements on the deuteron [7,9,10] are marked with diamonds, experiments using polarised Deuterium [11,12,13] or $^3\vec{\mathrm{He}}$ [15,30] targets are shown as circles and squares, respectively. Open triangles refer to the analysis [6] of unpolarised data. The thin full curve represents the original Galster parametrisation [5], the thick line represents the "pion-cloud" parametrisation [31] (see text). The dashed and dotted lines are discussed in the text.

with a smooth part

$$G_s(Q^2) = \frac{a_{10}}{(1+Q^2/a_{11})^2} + \frac{a_{20}}{(1+Q^2/a_{21})^2} \qquad (11)$$

and a bump

$$G_b(Q^2) = e^{-\frac{1}{2}(\frac{Q-Q_b}{\sigma_b})^2} + e^{-\frac{1}{2}(\frac{Q+Q_b}{\sigma_b})^2}\,, \qquad (12)$$

where $Q = \sqrt{Q^2}$. A fit to the current data yields the parameters $a_{10} = 1.2974$, $a_{20} = -a_{10}$ (for normalisation), $a_{11} = 1.73010$ $(\mathrm{GeV}/c)^2$ (fixed in the fit), $a_{21} = 1.54479$ $(\mathrm{GeV}/c)^2$, $a_b = 0.19426$ $(\mathrm{GeV}/c)^{-2}$, $Q_b = 0.34210$ GeV/c, and $\sigma_b = 0.16758$ GeV/c. The slow fall of $G_{E,n}$ at higher Q^2 is accommodated by the smooth part of the ansatz, eq. (11).

5 Nucleon Models

The elastic nucleon form factors present a significant test for nucleon models and most recent calculations aim to reproduce all four electromagnetic form factors with one set of adjustable parameters. Thus a full discussion of the predictive power of various models requires comparison with the complete elastic form factor data set. Such a comparison is beyond the scope of the present work and we confine our discussion to some recent calculations of $G_{E,n}$. The curves showing the predicted $G_{E,n}$ values (fig. 7) are labeled with the present reference of the particular calculation.

1. Nucleon models built upon basic assumptions and with a small number of free parameters include the semi-bosonized SU(3) Nambu–Jona-Lasinio model [32] and relativistic constituent quark models [33]. They are, in general, not able to provide a satisfactory description of all form factors, a fact which underlines the lack of understanding of the structure of the nucleon.
2. Generalised Parton Distributions (GPD) are considered to represent the momentum distributions of the constituents of the nucleon and the elastic form factors represent moments of particular GPDs. With a simple Regge ansatz for the Q^2-dependence of the GPDs H and E it is possible to reproduce experimental form factor data over a large range of Q^2 [3].
3. A recent vector dominance model [34] gives a reasonably good description of the four elastic proton and neutron form factors.
4. A dispersion-theoretical analysis [35] reproduces the trend of the electromagnetic form factors over a wide range of momentum transfers. At small Q^2 however it suggests values for $G_{E,n}$ which are significantly smaller than the measured data points.
5. The diquark-quark model of ref. [36] describes the measured $G_{E,n}$ at low Q^2, it misses however the trend of the data for $Q^2 > 0.4$ $(\mathrm{GeV}/c)^2$.
6. The chiral soliton model of ref. [37] falls far below the $G_{E,n}$ data for $Q^2 > 0.6$ $(\mathrm{GeV}/c)^2$. In addition, some of its parameters are clearly at variance with experiment, such as the anomalous magnetic moments of the proton and neutron.
7. Recent lattice QCD calculations in quenched approximation [38] qualitatively reproduce the trend of the data for the four electromagnetic nucleon form factors. Quantitative discrepancies, however, amount to a factor 2 in case of $G_{E,n}$.

6 Conclusion

The electric form factor of the neutron, $G_{E,n}$, has been measured at four-momentum transfers 0.3, 0.6, and 0.8 $(\mathrm{GeV}/c)^2$ in a double-polarisation experiment using a polarised electron beam and a final-state neutron polarimeter in the reaction $\mathrm{D}(\vec{e},e'\vec{n})p$. The ratio of transverse to longitudinal neutron polarisation components was measured by precession of the neutron spin in a magnetic field, which provided a cancellation of several systematic uncertainties. Nuclear binding effects have been corrected for using a model which gives an excellent account of a broad range of electron-deuteron reactions. The present experimental results are in good agreement with all other $G_{E,n}$ double-polarisation measurements.

Acknowledgements

We are highly indebted to the MAMI accelerator group and the MAMI polarised beam group for their outstanding performance. This work was supported by the Sonderforschungsbereich 443 of the Deutsche Forschungsgemeinschaft and by the UK Engineering and Physical Sciences Research Council.

References

1. F.J. Ernst, R.G. Sachs, K.C. Wali, Phys. Rev. **119**, 1105–1114 (1960).
2. N. Isgur, Phys. Rev. Lett. **83**, 272–275 (1999).
3. M. Vanderhaeghen, *Exclusive Processes at high momentum transfer*, (Eds. A. Radyushkin, P. Stoler, World Scientific, Singapore 2002), 51–56.
4. S. Platchkov *et al.*, Nucl. Phys. A **510**, 740–758 (1990).
5. S. Galster *et al.*, Nucl. Phys. B **32**, 221–237 (1971).
6. R. Schiavilla, I. Sick, Phys. Rev. C **64**, 041002 (2001).
7. T. Eden *et al.*, Phys. Rev. C **50**, 1749–1753 (1994).
8. M. Ostrick *et al.*, Phys. Rev. Lett. **83**, 276–279 (1999).
9. C. Herberg *et al.*, Eur. Phys. J. A **5**, 131–135 (1999).
10. R. Madey *et al.*, Phys. Rev. Lett. **91**, 122002 (2003).
11. I. Passchier *et al.*, Phys. Rev. Lett. **82**, 4988–4991 (1999).
12. H. Zhu *et al.*, Phys. Rev. Lett. **87**, 081801 (2001).
13. G. Warren *et al.*, Phys. Rev. Lett. **92**, 042301 (2004).
14. J. Becker *et al.*, Eur. Phys. J. A **6**, 329–344 (1999).
15. J. Bermuth *et al.*, Phys. Lett. B **564**, 199–204 (2003).
16. T. Eden *et al.*, Nucl. Instrum. Meth. A **338**, 432–441 (1994).
17. H. Arenhövel, W. Leidemann, E.L. Tomusiak, Z. Phys. A **331**, 123–138 (1988).
18. A.I. Akhiezer, M.P. Rekalo, Sov. J. Nucl. Phys. **4**, 277–287 (1974).
19. R.G. Arnold, C.E. Carlson, F. Gross, Phys. Rev. C **23**, 363–374 (1981).
20. T.N. Taddeucci *et al.*, Nucl. Instrum. Meth. A **241**, 448–460 (1985).
21. K.I. Blomqvist *et al.*, Nucl. Instrum. Meth. A **403**, 263–301 (1998).
22. Th. Pospischil *et al.*, Nucl. Instrum. Meth. A **483**, 713–725 (2002).
23. S.O. Grözinger, diploma thesis, Institut für Kernphysik, Mainz, Germany 2001.
24. M. Seimetz *et al.*, *A Neutron Polarimeter for the Three Spectrometer Setup at MAMI*, to be submitted to Nucl. Instrum. Meth. A.
25. R.A. Arndt, I.I. Strakovsky, R.L. Workman, Phys. Rev. C **62** (2000), 034005; `http://gwdac.phys.gwu.edu` .
26. O. von Strähle, diploma thesis, Institut für Kernphysik, Mainz, Germany 2000.
27. G. Kubon *et al.*, Phys. Lett. B **524**, 26–32 (2002).
28. A. Afanasev, I. Akushevich, N. Merenkov, Phys. Rev. D **64**, 113009 (2001).
29. M. Meyerhoff *et al.*, Phys. Lett. B **327**, 201–207 (1994).
30. J. Golak *et al.*, Phys. Rev. C **63**, 034006 (2001).
31. J. Friedrich, Th. Walcher, Eur. Phys. J. A **17**, 607–623 (2003).
32. H.-Ch. Kim, A. Blotz, M.V. Polyakov, K. Goeke, Phys. Rev. D **53**, 4013–4029 (1996).
33. D. Merten *et al.*, Eur. Phys. J. A **14**, 477–489 (2002).
34. E.L. Lomon, Phys. Rev. C **66**, 045501 (2002).
35. H.-W. Hammer, U.-G. Meißner, Eur. Phys. J. A **20**, 469–473 (2004).
36. B.-Q. Ma, D. Qing, I. Schmidt, Phys. Rev. C **65**, 035205 (2002).
37. G. Holzwarth, hep-ph/0201138.
38. J.D. Ashley, D.B. Leinweber, A.W. Thomas, R.D. Young, Eur. Phys. J. A **19**, 9–14 (2004).